Central European Journal of Energetic Materials
ISSN 1733-7178; e-ISSN 2353-1843

Cent. Eur. J. Energ. Mater. 2024, *21*(2): 188-209; DOI 10.22211/cejem/190549
Article is available in PDF-format, in colour, at:
https://ipo.lukasiewicz.gov.pl/wydawnictwa/cejem-woluminy/vol-21-nr-2/

Research paper

Explosively Formed Penetrators Inflight Heating Compared to Hemispherical Copper Shaped Charge Jet

Sherif M. Abdelkhalek[1)], **Mahmoud Abdelhafiz**[2)], **Shukri Ismael**[2)], **Sherif Elbasuney**[2)], **Tamer Elshenawy**[3,*)]

[1)] *Engineering and Technology Research Center, Military Technical College, Cairo, Egypt*

[2)] *School of Chemical Engineering, Military Technical College, Cairo, Egypt*

[3)] *Technical Research Centre, Cairo, Egypt*

**E-mail:* tamershenawy@yahoo.com

Abstract: Performance of shaped charges jet and explosive formed penetrators (EFP) can be tailored based on initial liner design and geometry. In addition, the jet temperature gradients during liner collapse and jet stretching mechanisms are different in both cases; the EFP and the traditional jet due to the different strain rates caused by the velocity gradient. In the current research work, oxygen free high conductivity copper (OFHC) was employed with two different liner geoemtries including hemispherical and dish-shaped liners of 2 mm thickness and 33 mm charge diameter. Autodyn numerical modeling was employed to study the impact of liner geometry on the characteristics of produced jet. Moreover, the jet heating mechanisms have been investigated numerically; the ratio between the collapse heating temperature to the plastic deformation temperature was found to be 1.61 and 0.43 for the dish-shaped and hemispherical jet respectively. This finding means that the jet heating due to stretching is not predominant one in both EFP and jet as it has already been confirmed in the papers published so far. Furthermore, EFP and jet penetration performances were assessed by the static firing against 4340 steel targets; while dish-shaped demonstrated shallow but enhanced wide crater at large standoff distance (D), *i.e.* 30D. Hemispherical jet has achieved large penetration depth with small crater diameter at small standoff distance, *i.e.* 4D.

Keywords: hollow charge, explosively formed penetrators, jet temperature, penetration, copper liner

1 Introduction

Shaped charge performance is evaluated based on the penetration depth and crater diameter inside the target material. The liner material and geometry are the main controlling parameters that determine the shape of the generated jet. Figure 1 demonstrates the impact of liner geometry on jet formation and its shape, whatever shaped charge traditional jet or EFP. Althought the shaped charge phenomenon has been discovered over 100 years ago, other aspects such as jet heating still needs further investigations and research [1]. One of these issues is the thermodynamics of the shaped charge jet during its stretching and during the early stages of jet formation. The mechanisms of jet formation in both traditional jet and EFP are expected to be completely different.

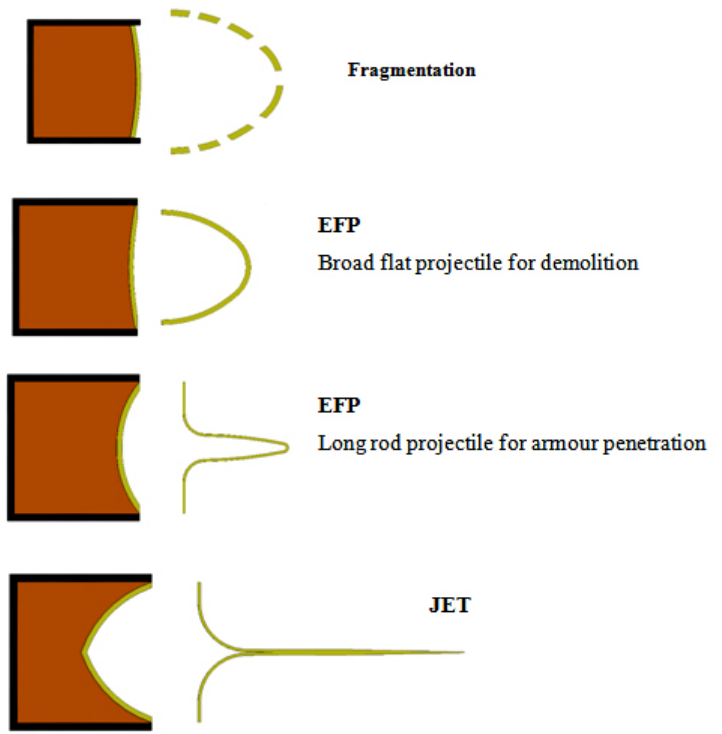

Figure 1. Jet formation as function of liner geometry

Pai *et al.* [2] has made an attempt to measure the temperature of EFP using thermoelectric effect by thermocouple. The velocity of the EFP was found to be 2.7 km/s, whereas the temperature increase of the generated EFP was found to be 600 ±60 °C over its cross-section.

Pai *et al.* [3] tried three layers copper/copper/constantan cladding configuration as an attempt to simulate shaped charge of base diameter 40 mm and liner angle is 45° and wall thickness of 1.5 mm to measure its jet temperature. The inner copper was driven by RDX explosive charge of thickness of 20 mm. The resultant jet was allowed to impact on a thermocouple at stand-off distance of 0.6CD (*i.e.* six times charge diameter) to record the jet temperature over its cross-section. Oscilloscope was employed to measure the potential difference between the jet tip and its tail. The analysed oscilloscope thermo signal recordings showed potential difference corresponding to a copper jet temperature of 800 ±80 °C.

Von Holle and Trimble [4] measured the temperature of shaped charge copper jet of diameter 81.3 mm with Composition B (RDX/TNT 60/40) explosive charges. The measured average jet temperature at travelling distance of eight times charge diameter was found 432 °C with a standard deviation of 76 °C. Racah [5] discussed the three different mechanisms of liner heating during the explosive grazing, liner collapse, and jet stretching. The first mechanism is the liner heating by the detonation wave as it grazes the liner. The calculated temperature for this mechanism is 30 °C for the copper liner. The second mechanism is the liner heating during the liner collapse process. The third mechanism is the jet heating during its stretching.

Elshenawy and Elbasuney [6] discussed the jet temperature distribution of a small diameter 40 mm shaped charges including zirconium and OFHC copper liners. Numerical study using Autodyn hydrocode was adopted to record the temperature histories around the loop direction in both cases; zirconium and baseline copper liners. It was found that zirconium had a superior average jet collapse to plastic deformation temperature ratio of 0.73 compared with 0.34 for the baseline oxygen free high conductivity copper (OFHC). This finding has been attributed to the difference in the strain rate values obtained during the jet stretching stages and also attributed to the pyrophoric nature of the zirconium material rather than the copper one. Significant difference values for the corresponding temperature incresae in both mechanisms of jet and liner collapse heatings for both studied liner types have been addressed.

On the other hand, hemispercal liners has attracted interest as they can experience high jet mass and low off-axis drift velocities at extended stand-off distances compared with traditional conical shape [7]. Furthermore different liner geometry can offer different crater depth and diameter during penetration testing.

However, limited researches have been carried out to measure the temperature of the produced jet and EFP. Better understanding of this jet heating will clarify the jet softening and its breaking up during the stretching phase.

Many trials have been carried out to measure the jet temperature [3] and numerically estimate this temperature for conical liners [8]. Babkin *et al.* [9] studied the effect of the liner heating and its accompanied thermal effect on the jet plastic deformation and relevant failure during the jet stretching and its penetration. Sable *et al.* [11] numerically discussed the shaped charge jet inflight heating and validated previous testing results when compared to CTH hydrocode. Flis [12] discussed theoretically the temperature increase of both the jet and the target due to its penetration with and without the strength model and with the consideration of shock compressibility.

Based on the discussed researches, it was concluded that it is necessary to understand the thermodynamic aspect of both the jet and the the EFP during their formation and to investigate this temperature increase during the three mechanisms during the jet formation in both cases. Moreover, two different liner geometries including hemispherical and dish-shaped were also investigated. Numerical modeling using Autodyn hydrocode was performed to study the effect of liner geometry on the coherency of the produced jet and its characteristics. Numerical hydrocode was also implemented to assess the performance of both jets associated with liner geometry depending on the obtained jet temperature and optimum stand-off distance. The performance of these two liners have been assessed via static firing of the two shaped charges including two developed liners against 4340 steel targets. The penetration depth and the crater diameter of the produced jet have also been considered.

2 Experimental

Ductile jet material is necessary to maintain extended breakup time as well as improved consistent performance [13]. The employed liner material was OFHC, grade C10100. Copper purity was 99.99 %, with low oxygen and phosphorus contents. C10100 has a minimum 101% IACS (International Annealed Copper Standard) conductivity rating. Chemical composition of employed copper obtained by spectrum analysis and is tabulated in Table 1. Copper was proceesed to the final shape in controlled oxygen-free environment.

Table 1. The chemical composition of copper alloy C10100 grade

Element	Cu	Pb	Zn	Fe	P	Ag	As	Sb	Te
Impurities amount [%]	99.99	0.0005	0.0001	0.0010	0.0003	0.0025	0.0005	0.0004	0.0002

Copper liners geometry, thickness, and dimensions are demonstrated in Figures 2(a) and 2(b). Copper liners were manufactured by turning technique using high precision CNC machine (5 μm precision) (Figure 2(c)).

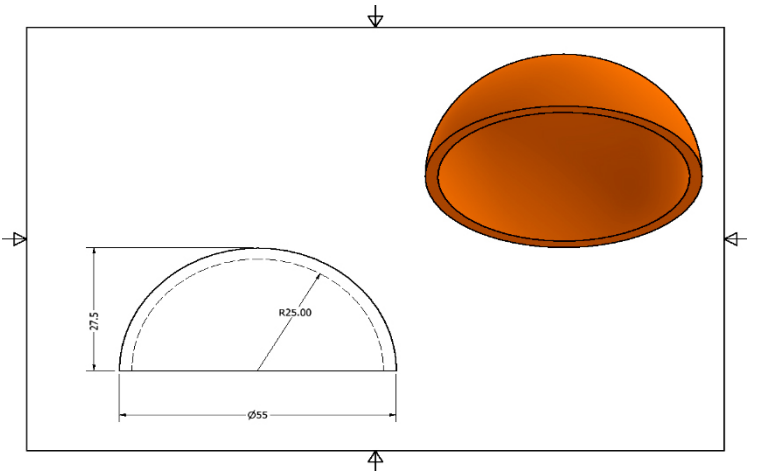

(a)

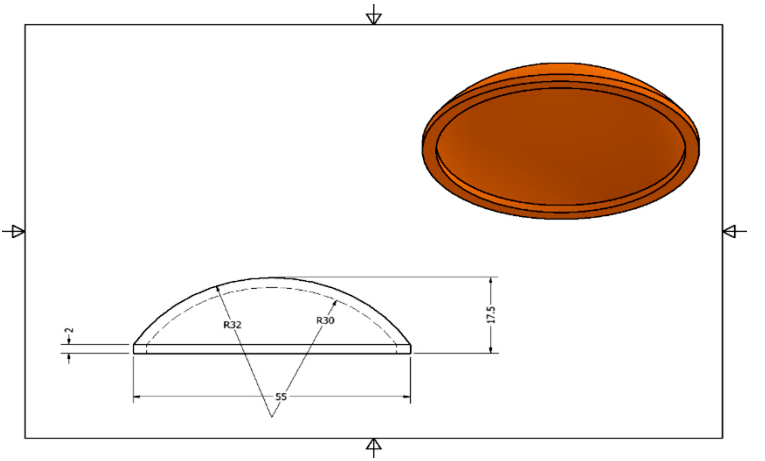

(b)

(c)

Figure 2. Dimestions and geometry of hemispherical (a), dish-shaped liner (b), manufactured hemispherical and dish-shaped liners (c)

Explosive charge of 50 g of Composition B was employed. TNT was melted in a steam-jacketed kettle. RDX was added in four portions with stirring. Composition B experienced an average density density of 1590-1620 kg/m^3, and detonation velocity of 7836 m/s.

Table 2. The detonation characteristics of the used explosive load [13]

Sample	Loading density [kg/m^3]	Detonation velocity [m s^{-1}]	Detonation pressure [kPa]	C-J energy per unit volume [kJ/m^3]
Composition B	1620	7836	2.40×10^7	9.204×10^6

Shaped charges were loaded with 50 g Composition B was assembled in thick PVC tube to maintain the required stand-off distance. Assembled shaped charge was attached to AISI 4340 steel target, pre-annealed at 810 °C. Heat treated steel target experienced yield strength of 470 MPa. Different stand-off distances were investigated to achieve optimum penetration of 4340 steel target (Figure 3). Stand-off distance according to liner geometry was evaluated using Autodyn hydrocode. Optimum stand-off distance that could maintain continous jet penetrating during crater formation was optimized according liner geometry.

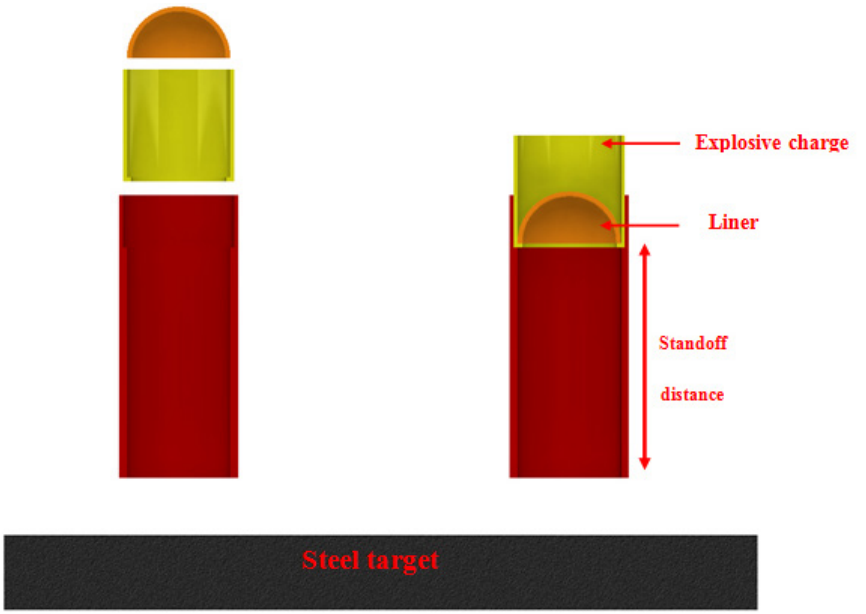

Figure 3. The experimental penetration test setup

3 Numerical Calculations

3.1 Autodyn numerical hydrocode

Generally, three different schemes including jetting analysis, jet formation, and jet interaction with the steel target (penetration) have been implemented within Autodyn numerical hydrocode. The jetting analysis (based on unsteady state PER theory) was employed to calculate masses and velocities of jet and slug; as well as the resultant kinetic energy and jet momentum [14]. The collapse, flow and jet velocities, the liner collapse, deflection angles, and jet kinetic energy were estimated. Jet radius and elemental break-up time were estimated based on the output standard jetting analysis [14]. Jet formation was performed using Euler solver based on continuum mechanics to obtain the jet profiles at different time stages [15]. The output of this scheme (jet having certain momentum at certain time) was employed as the input of Lagrange-Lagrange jet-target interaction scheme.

Jet penetration into steel target was modeled using Lagrange method. In this scheme, the obtained jet was remapped to Lagrangian moving grids and impacts the steel target. The overall crater profile inside the steel target could be

monitored. The overall mesh sizes in both Euler jet formation and Lagrangian jet and target have been used as a square mesh of size 0.2 mm each. An outflow boundary condition has been implemented to the the last I and J lines to allow expanded detonation products to flow out the limited part without reflecting back to the main part. On the other hand, the optimized erosion strain values have been used as 4 for shaped charge jet and 0.4 for the target materials; respectively. Further details such as erosion strain effect and mesh sensitivity analysis as well as validity and verification of the following reference [16].

3.2 Material model

The equation of state (EOS) for employed high explosive is Jones-Wilkins-Lee (JWL) equation. Experimental constants, for emplyed explosives, have been determined from sideways plate push dynamic test experiments [17] and the cylinder expansion test [13, 18, 19]. Composition B explosive loading density was 1.62 g/cm^3. Parameters in the JWL EOS equation equal $A = 8.1658\times10^8$ kPa, $B = 1.6228\times10^7$ kPa, $\omega = 0.185$, $R_1 = 4.067$ and $R_2 = 1.377$. Detonation velocity and pressure equal to 7836 m/s and 2.40×10^7 kPa, respectively. The C-J energy per unit volume equals 9.204×10^6 kJ/m^3. The detonation characteristics were obtained from [20].

The copper liner material has density of 8.9 g/cm^3. Copper was modeled by linear EOS of bulk modulus 1.0×10^8 kPa and reference temperature of 293 K. The adopted strength model was Johnson Cook (J-C) (Equation 1).

$$\sigma = (A + B\varepsilon^n)(1 + Cln\dot{\varepsilon}^*)(1 - T_H^m) \tag{1}$$

where σ, ε, A, B, n, C and m are dynamic flow stress, effective plastic strain, yield strength, hardening constant, hardening exponent, strain-rate constant, and thermal exponent constant, respectively, $\dot{\varepsilon}^*$ is the normalized effective plastic strain-rate (*i.e.* the applied true strain-rate divided by the reference strain-rate). T_H is the homologous temperature that can be calculated using Equation 2.

$$T_H = \frac{T - T_{room}}{T_{melt} - T_{room}} \tag{2}$$

where T_{room}, T_{melt} are room temperature, and melting temperature respectively. The J-C constants for the copper material are listed in Table 3. The Mie-Gruneisen thermodynamic form describes the heat capacity variations and thermodynamic properties with a reference temperature of 300 K and heat capacity 3.8310^{-4} J/Kg·K for the copper liner material [8].

Table 3. The material model and the mechanical properties of the used liner materials [20]

Parameter	Copper
Reference density [g/cm^3]	8.93
A [MPa]	90
B [MPa]	292
n	0.31
C	0.025
m	1.09
$\dot{\varepsilon}_0$	1
Parameter C [m/s]	3958
Parameter S	1.497
Ref. temperature [K]	300
Heat capacity [J/Kg K]	3.83×10^{-4}

Explosive charge case was PVC of 0.915 g/cm^3 density with the shock EOS of parameters $C = 2901$ m/s and $S = 1.481$. The steel target material has a density of 7.86 g/cm^3 and shock EOS of Gruneisen coefficient 1.67 and parameter $C = 4397$ m/s and $S = 1.73$. The strength model adopted with the steel target is the von Mises criteria of shear modulus 74 GPa, and yield stress of 470 MPa. The material parameters of the target are listed in Table 4.

Table 4. Properties of casing and steel target materials [15]

Parameter	PVC	Steel targets hardness, HB 217
Equation of state	**Shock**	**Shock**
Reference density [g/cm^3]	0.915	7.86
Gruneisen coefficient	1.64	1.67
Parameter C [m/s]	2901	4397
Parameter S	1.481	1.73
Ref. temperature [K]	300	300
Strength model	**None**	**von Mises**
Shear modulous [GPa]	-	74
Yield strength [MPa]	-	470

4. Results and Discussions

4.1 The jet characteristics

The behaviours of the momentum history of both liners (dish-shaped and the hemispherical) are represented in Figure 4. Both histories demonstrated similar exponential increase in the liner moementum with different magnitudes. The hemispherical liner history showed maximum momentum of 2.5×10^4 g·m/s, whereas the dish-shaped one demnonstrated lower value of 1.7×10^4 g·m/s. However, the dish-shaped liner gains its maximum stable momentum at about 15 µs, which is faster than that of the hemispherical one, which is 25 µs. This may be attributed to the larger surface area of the hemispherical liner compared to the dish-shaped, which may needs longer time to collpase under the action of the detonation pressure load. Such difference is expected to appear as discussed in [21], which exhibited performance dependance on the EFP radius.

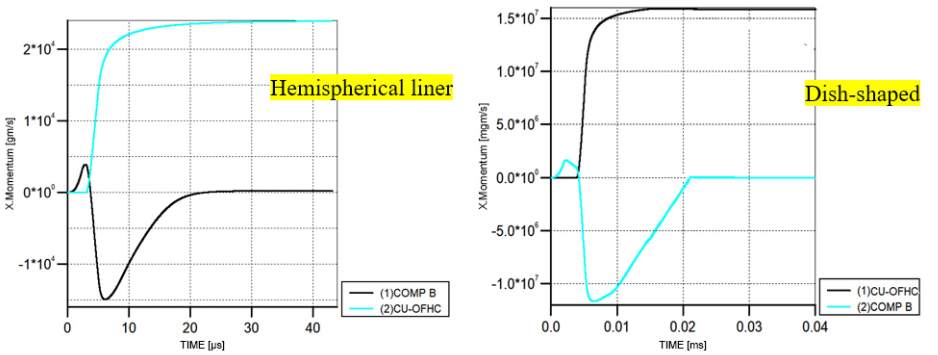

Figure 4. The momentum history of hemsipherical and dish-shaped liners

The efficiency of the shaped charge liner performance is determined according to its penetration potential achieved into the studied steel target. The penetration performance mainly depends upon the jet tip velocity, the cutoff velocity, the breakup time and the jet material in addition to other parametrs such as jet symmetry and drift from the main jet axis. The jet velocity and its gradient are so important that they determine the jet breakup time and its ductility. The jet velocity contours for hemispherical and dish-shaped liners were investigated. The hemispherical jet has a thick diameter with a tip velocity around 3800 m/s whereras the rear velocity exhibits a lower value of 1000 m/s. The jet diameter decreases as the jet stretches untill it breaks up into small fragments. Consequently, the penetration decresaes dramatically, and the jet does not become effective anymore. This means that the stand-off distance is effective in this

case and the jet continuity is of great importance. Jet continuity was monitored carefully untill its breaking up (Figure 5). On the other hand, the dish-shaped liner demonstrated a massive EFP with a tip velocity around 2550 m/s, whereas its rear element veloctity is about 1962 m/s. After certain time and due to strain hardening, only small fragments split off the massive EFP. Such fragments move with uniform velocity until reaching the target surface (Figure 6).

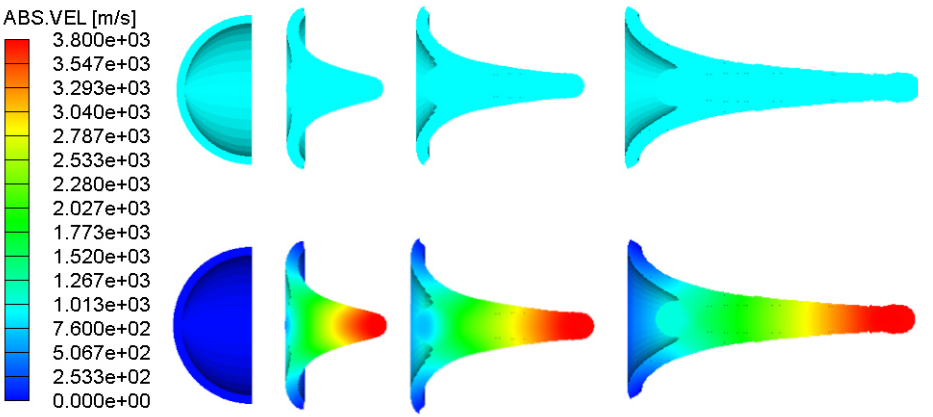

Figure 5. The jet profile and its velocity at 0, 20, 28, and 38 μs for hemispherical liner

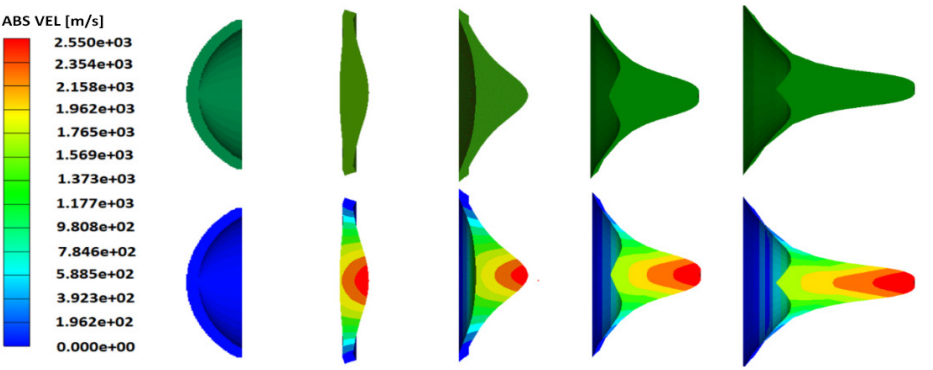

Figure 6. The copper dish-shaped liner profile and its velocity at 0, 10.1, 15.8, 25.7 and 30 μs

This is expected due to EFP phenomenology as discussed in [22]. The mass percent in this case is greater than that of the hemspherical jet and approximating 85% of the initial liner mass. In addition, due to the lower velocity gradient and

due to the strain hardening in the flyer dish-shaped in air, the larger diameter of the dish-shaped decreases slowly until the dish-shaped keeps its final shape during most of the flight travel. Generally, although dish-shaped diameter seems to be more or the same as the hemisperical jet at the begining of the jet formation; this difference becomes significant as the jet stretches and become thinner as long as it travels through the air. This behaviour is different from that of the massive slug moving with uniform velocity EFP projectile. The jetting characteristics for both liner designs are represented in Table 5.

Table 5. The jetting calculation outputs for the baseline OFHC copper jet and EFP

Liner geometry	Hemisperical	Dish-Shaped
Liner mass [g]	28.6	20.2
Jet mass [g]	14.9	17.2
Jet percentage [%]	52	85
Jet kinetic energy [kJ]	17.3	14.2
Maximum jet tip velocity [m/s]	3886	2550
Maximum flow velocity [m/s]	1786	1520

4.2 Jet temperature calculation

The estimation of the jet temperature is necessary to assess the overall behind armor effect [23] and the jet thermal softening phenomena during liner collapse and jet stretching in air. The shaped charge jet heating is considered as the most important issue during the jet formation, where it takes part in the softening of the jet and related particulation during travel distance [5]. Thus, the shaped charge jet heating during the plastic deformation is therefore an important issue to be studied numerically due to the difficulty in practical measurements. Three different mechanisms could withstand jet heating including liner grazing by the detonation wave of the explosive, the liner heating during the its collapse process, and the heating due to the platic deformation during the jet stretching.

It was found that the third mechanism is the predomninat one and have the largest impact on the jet heating [5]. Thus, Autodyn hydrocode was employed to investigate the jet heating during the shaped charge jet formation via the Mei-Gruneisen thermodynamic model based on shock equation of state for the OFHC copper material for both liners [24].

The jet temperature calculations during the liner collapse and the jet stretching using Autodyn have been validated and compared to the measured one with quite similar results [24, 25]. This will not be revalidated again within our research.

In an attempt to calculate the temperature of the jet at different locations, few moving gauge points were assigned within the liner elements to investigate the temperature around the loop of the jet and EFP cores. The temperature histories of these gauge points were then recoded from the starting time until the jet/EFP was fully stretched and the temperature increase reached its steady state constant value. The location of the selected moving gauge points are represented for dish-shaped liner (Figure 7).

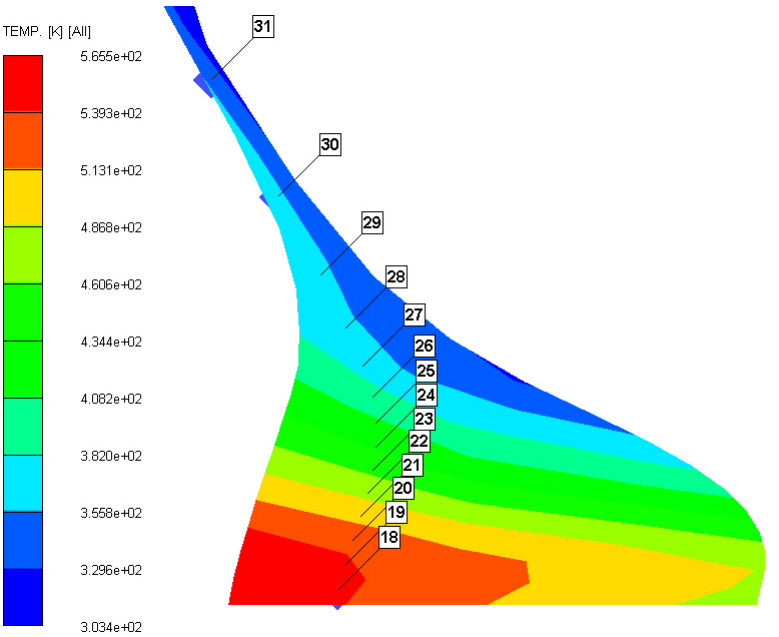

Figure 7. The loacation of the moving gaue points inside the dish-shaped liners

Jet behavhiors and jet heating started from time 0 μs as well as during stretching condition, until it reached steady state. It was found that the temperature across the jet/EFP width varies outward. The highest temperature was found at the inner core of the jet/EFP but decreases gradually at the outer surface. The same phenomena have been observed for both the EFP and the traditional thin jet although they exhibit different temperature magnitude and various temperature contour regions.

In order to quantify the values of both the two mechanisms responsible for jet and EFP heating, the assigned gauges located at different locations shown in Figure 7 are allowed to recored the temperature histories until reaching steady states as depicted in Figure 8.

The two mechanisms responsible for the jet heating are the liner heating during collapse process (denoted by collapse process heating (CPH)) and the liner heating during the jet stretching and the plastic deformation (denoted by plastic deformation heating (PDH)).

The first peak represented in Figure 8 shows the heating due to the dish collapse, CPH, which lasts only less than 1 ms for the entire gauges. After this temperature increase, it decresases suddenly until it reached the steady state value that represents the plastic deformation heating. This value was lower than that of the CPH due to limited stretching relevant velocity gradient of the formed EFP when compared to the same case of shaped charge jet during the same state of traditional jet. This fact contradicts that work of Racah [5], who generalized that fact for the shaped charge jet, in which the PDH is much higher than that of the CPH. Similar to EFP temperature heating, the jet formed from hemispherical liner is allowed stretch until the temperature contours appeared via output results as depicted in Figure 9.

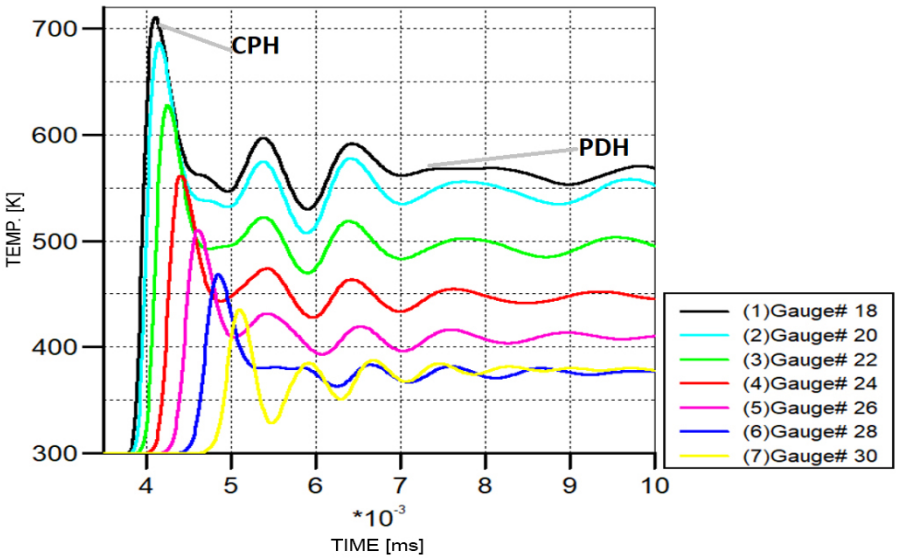

Figure 8. The calculated temperature along the EFP loop direction

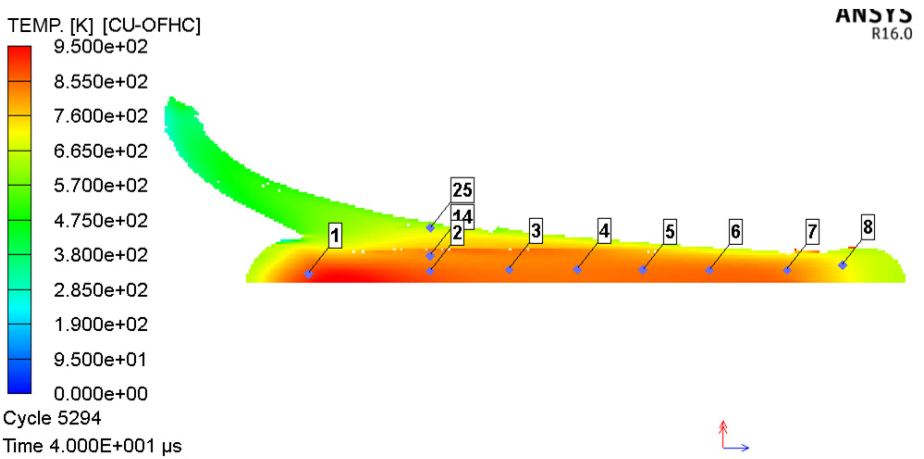

Figure 9. The loacation of the moving gaue points inside the OFHC copper jet of the hemispherical liner

The output temperature histories for some gauge points are demonstrated in Figure 10 for the hemispherical jet material. The jet heating due to liner collapse (CPH) can be observed to be much lower than that caused by the jet stretching (PDH) (*i.e.* about one third its value). This is different from the behaviour of the previous studied EFP. This can be attributed to the ultra strain rate caused by the jet, which is mainly caused by the velocity gradient at both the jet tip and its tail elements.

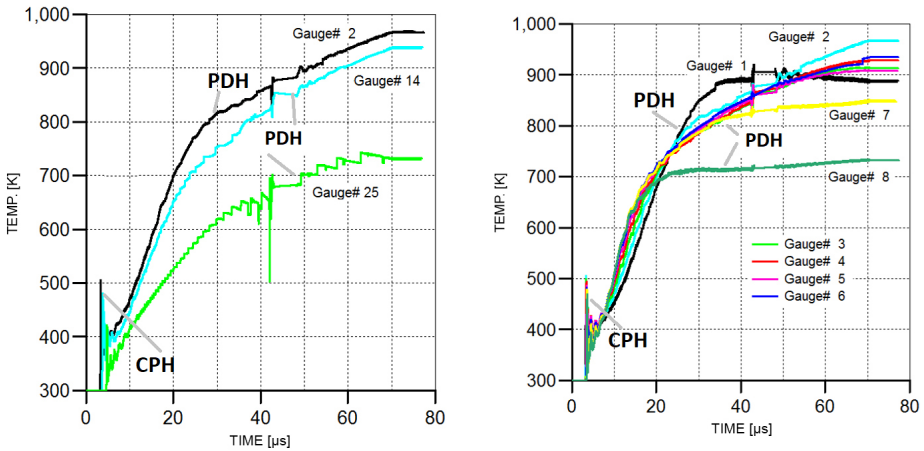

Figure 10. The calculated temperature along the jet length and its loop for the OFHC copper hemispherical liner

The maximum temperature was recorded for each gauge point separately and listed in Table 6 for investigated two liners. It was concluded from Table 6 for the dish-shaped, that the most of the gauges show ratios between the collapse to the plastic deformation temperatures of 1.48 to 1.91 with the largest obtained value near the charge axis, whereas the hemispherical copper jet exhibits lower values between 0.31 to 0.42 with an average value of 0.34. This difference between the dish-shaped and jet may be caused by the difference in the jet velocities in both cases. This could result in different strain rates and therefore different temperature increase values for both mechanisms in both dish-shaped and jet. Generally, most of the jet elements in case of copper hemispherical liner shows higher temperature than those in the dish-shaped. On the other hand, the heat generated from the plastic deformation mechanism in case of dish-shaped is about 63% that the value of the collapse process, which seems to be almost equal to that corresponding values in case of the hemispherical jet but due to the lower dish-shaped homogeneous velocity, the stretching is limited and therefore the plastic deformation temperature increase is limited in case of dish-shaped. This fact shows that the impact of the three heating mechanisms is not always the same in both the dish-shaped EFP and the traditional jet, besides, the temperature obtained from the dish-shaped projectiles does not encourage its use when behind armour effect is most considerable.

Table 6. The summary of the collapse and plastic deformation heating temperatures for copper EFP and jet

Copper EFP [°C] (dish-shaped liner)				Copper jet [°C] (hemispherical liner)			
Gauge	T-Collapse	T-Plast. Def.	T-Collapse /T-Plast. Def.	Gauge	T-Collapse	T-Plast. Def.	T-Collapse /T-Plast. Def.
18	437.6	287.5	1.52	1	231	646.8	0.36
19	433.2	292.8	1.48	2	232	694.5	0.33
20	413.3	277.8	1.49	3	225	641.4	0.35
21	386.8	261.6	1.48	4	220	655.3	0.34
22	354.6	217.7	1.63	5	212	636.3	0.33
23	321.8	202.2	1.59	6	207	661.6	0.31
24	288.1	177.2	1.63	7	205	576.1	0.36
26	237.3	142.8	1.66	8	196	461.4	0.42
28	195.3	102.1	1.91	14	205	666.3	0.31
30	162	97.4	1.66	25	147	469.5	0.31

4.3 The penetration testing

The remapped jet and EFP obtained from Euler solvers were allowed to impact on the 4340 steel target at the designated stand-off distance, whereas the total penetration depth was calculated either when the jet is totally consumed on the crater walls or when its velocity falls below certain value termed as cut-off velocity. The penetration craters for the EFP are shown in Figure 11 at different stand-off distances of 1D, 3D, 4D, 5D and 10D respectively. Crater profile reveals the preliminary shape of the expected EFP as it is formed with a large diameter at the beginning (*i.e.* 1D to 5D), after which the EFP diameter almost remains constant, which shows mximum constant penetration depth at large stand-off distance greater than 10D. The final achieved penetration at this large stand-off distance equals to 41 mm (*i.e.* about 1.3D), which remains constant at very large stand-off distance of 30D.

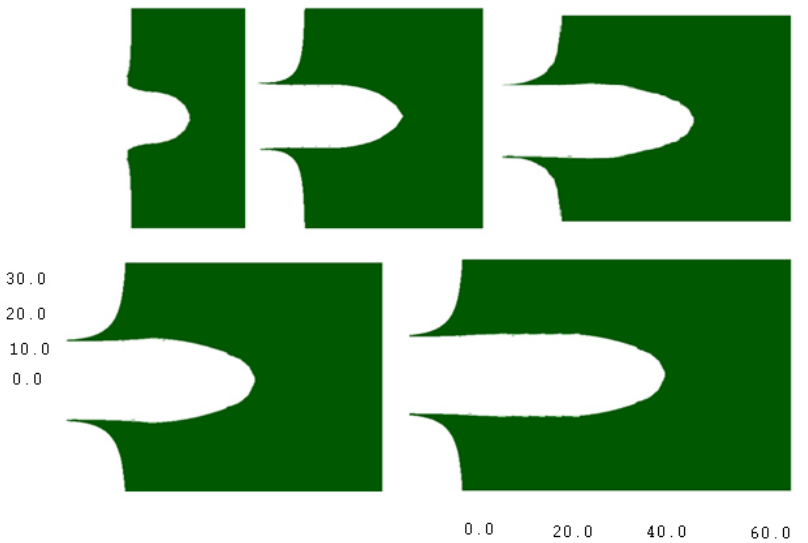

Figure 11. The numerical crater profile inside steel target for the dish-shaed liner, penetration at different standoff distances at 1D, 3D, 4D, 5D and 10D

The shaped charge jet shows different behviour depending on the jet sensitivity to the breakup phenomenon, which has a direct influence to the jet elongation prior to penetration into target material. The average breakup time of the jet tip is about 40 μs based on the jetting analysis calculations. This breakup determines the stand-off distance that must not be exceeded in order

to obtain maximum effective jet length and thus maximum penetration depth into steel target material. Figure 12 shows the crater profiles at different stand-off distances. It can be concluded from this figure that the optimum stand-off distance for this jet before the beginning of its breakup is four times the caliber. After this SOD, the penetration potential decreases dramatically due to the jet particulation and insufficient dynamic ductility, which is much affected by the thermal softening related to temperature increase and jet heating. This breakup time was approximated based on the current temperature of the jet as discussed by many researcher such as Elshenawy for ultrafine copper grains [26] and zirconium liners [24] and many researchers [27-29].

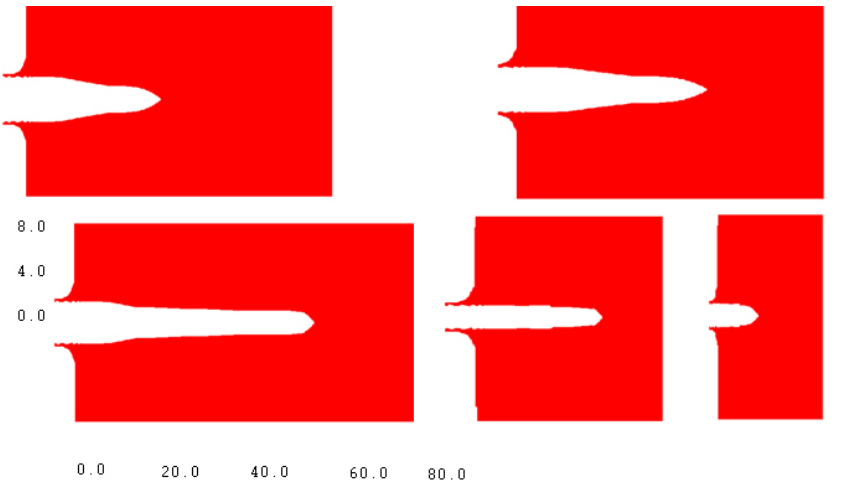

Figure 12. The numerical crater profile inside steel target for the hemispherical jet at 1D, 3D, 4D, 5D and 10D

Based on the discussed EFP and jet penetration, it can be concluded that the dish-shaped liner exhibited lower penetration than that of the traditional jet, but it has two main advantages such as the larger exit hole diameter and the guaranted penetration at larger stand-off distances (30 times charge caliber). This conclusion was assessed by Figure 13, which shows the penetration-stand-off curve at various stand-off distances for both liners.

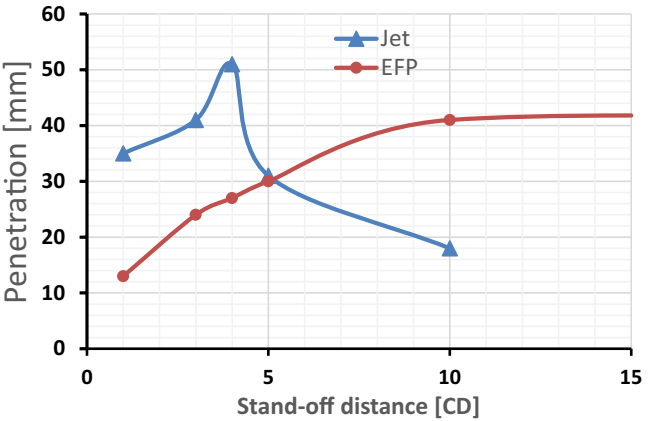

Figure 13. The penetration-standoff for both the jet and the EFP

Besides, the exit hole diameter is summarized in Table 7 for investigated two liners. It showed that lower dependence of the jet on the stand-off distance than that in case of the EFP projectile. The reason behind this finding is that the small diameter of the jet which does not exceeds few mm in the beginging of jet formation before the breakup starts.

On the other hand, the EFP has a big diameter at the beining of the EFP formation, which is about 20 mm and become thinner as it travels certain distances in air. The final shape of the EFP determines the shape of the produced crater inside the target material, which reveals great dependence on the EFP shape.

Table 7. Penetration depth and the exit hole diamters for both the copper jet and EFP at different standoff distances

SOD	Depth of penetration [mm]		Exit hole diameter EHD [mm]	
	Hemispherical jet	Dish-shaped EFP	Hemispherical jet	Dish-shaped EFP
1 D	35	13		18
3 D	41	24		20
4 D	50	27	7	23
5 D	31	30		23
10D	18	40		23

A halfway section of the penetrated steel by both the hemispherical liner jet and the EFP dish shaped liners is shown in Figure 14 for both experimental testings. It can be concluded that these profiles are similar to the crater profiles obtained by the numerical solution which validates the used Audtodyn hydrocode.

Besides, the achieved error between the experimental penetration and the numerical one is about 2%.

Figure 14. The experimental penetration for both the jet (left) and the EFP (right)

5 Conclusions

- Two similar shaped charges containing different copper shapes; hemispherical and dish-shape like liners have been studied theoretically and numerically. Relevant analysis for both shaped charges has revealed that hemispherical copper liner can achieve 24% larger penetration depth compared to the dish-EFP one. Besides, calculated radial crater analysis and verified experiments showed that the EFP has achieved 200-300% excess in the crater diameter compared to the hemispherical jet.
- Additionally, the numerical calculations of jet temperature showed that the heating mechanism for both copper jet and EFP is similar during the collapse process but begins to differ when the stretching starts, where the collapsed elements reach the centreline.
- The ratio between the collapse heating temperature to that of the the plastic deformation was found to be 1.61 for the EFP and 0.43 for the hemispherical jet, which is investigated within jet and EFP numerically. This fact was verified by the Racah [5] only in case of the jet, but the EFP heating mechanism showed different attitude due to its limited strain rate.

References

[1] Held, M. Liners for Shaped Charges. *J. Battlefield Technol.* **2001**, *4*(3): 1-6.
[2] Pai, V.V.; Kuz'min, G.J.C. Experimental Determination of Temperature of a Metal Jet. *Explosion Shock Waves* **1994**, *30*(3): 346-349.
[3] Pai, V.V.; Titov, V.M.; Luk'yanov, Y.L.; Zubashevski, K.M. Temperature Measurement of the Shaped-Charge Jet from a Conical Liner. *Combust. Explos. Shock Waves* **2020**, *56*(3): 361-364l https://doi.org/10.1134/S0010508220030132.
[4] Von Holle, W.G.; Trimble, J.J. Temperature Measurement of Shocked Copper Plates and Shaped Charge Jets by Two Color IR Radiometry. *J. Appl. Phys.* **1976**, *47*(6): 2391-2394; https://doi.org/10.1063/1.323028.
[5] Racah, E. Shaped Charge Jet Heating. *Propellants Explos. Pyrotech.* **1988**, *13*(6): 178-182; https://doi.org/10.1002/prep.19880130605.
[6] Elshenawy, T.A.E.; Elbasuney, S. Hemispherical Zirconium Liner for Advanced Shaped Charge with Enhanced Behind Armour Effect. *Cent. Eur. J. Energ. Mater.* **2021**, *18*(3): 293-321; https://doi.org/10.22211/cejem/140074.
[7] Whelan, A.J.; Furnisss, D.R.; Townsley, R.G. Experimental and Simulated (Analytical and Numerical) Elliptical-form Shaped Charges. *Proc. 20th Int. Symp. Ballistics,* Florida, **2002**.
[8] Agu, H. *The Effects of 3D Printed Material Properties on Shaped Charge Liner Performance*. Cranfield University, **2019**.
[9] Babkin, A.; Bondarenko, P.A.; Fedorov, S.V.; Ladov, S.V.; Kolpakov, V.I.; Andreev, S.G. Limits of Increasing the Penetration of Shaped-Charge Jets by Pulsed Thermal Action on Shaped-Charge Liners. *Combust. Explos. Shock Waves* **2001**, *37*: 727-733; https://doi.org/10.1023/A:1012948702419.
[10] Sable, P.; Helminiak, N.S.; Gullerund, A.; Harstad, E.; Hollenshead, J.; Hertel, E.S. Characterizing In-Flight Temperature of Shaped Charge Penetrators in CTH. *Procedia Eng.* **2017**, *204*: 375-382; https://doi.org/10.1016/j.proeng.2017.09.782.
[11] Flis, W.J. On Temperatures in Shaped-Charge Jet Penetration. *Proc. 30th Int. Symp. Ballistics*, **2018**.
[12] Schwartz, A.; Kumar, M.; Lassila, D. Analysis of Intergranular Impurity Concentration and the Effects on the Ductility of Copper-Shaped Charge Jets. *Metall. Mater. Trans. A* **2004**, *35*(9): 2567-2573; https://doi.org/10.1007/s11661-004-0203-8.
[13] Kato, H.; Kaho, N.; Takizuka, M.; Hamashima, H.; Itoh, S. Research on the JWL Parameters of Several Kinds of Explosives. *Mater. Sci. Forum* **2004**, *465-466*: 271-276; https://doi.org/10.4028/www.scientific.net/MSF.465-466.271.
[14] Pugh, E.M.; Eichelberger, R.J.; Rostoker, N. Theory of Jet Formation by Charges with Lined Conical Cavities. *J. Appl. Phys.* **1952**, *23*(5): 532-536; https://doi.org/10.1063/1.1702246.
[15] Team, A. *Autodyn Theory Manual*. Century Dynamics: CA, **1997**.
[16] Elshenawy, T.; Li, Q.M. Influences of Target Strength and Confinement on the Penetration Depth of an Oil Well Perforator. *Int. J. Impact Eng.* **2013**, *54*: 130-137;

https://doi.org/10.1016/j.ijimpeng.2012.10.010.
[17] Tarver, C.M.; Tao, W.C.; Lee, C.G. Sideways Plate Push Test for Detonating Solid Explosives. *Propellants Explos. Pyrotech.* **1996**, *21*(5): 238-246; https://doi.org/10.1002/prep.19960210506.
[18] Lan, I., Jung, S.C.; Chen, C.Y.; Niu, Y.M.; Shiuan, J.H. An Improved Simple Method of Deducing JWL Parameters from Cylinder Expansion Test. *Propellants Explos. Pyrotech.* **1993**, *18*(1): 18-24; https://doi.org/10.1002/prep.19930180104.
[19] Elek, P.M.; Džingalašević, V.V.; Jaramaz, S.S.; Micković, D.M. Determination of Detonation Products Equation of State from Cylinder Test: Analytical Model and Numerical Analysis. *Therm. Sci.* **2015**, *19*(1): 35-48; https://doi.org/10.2298/TSCI121029138E.
[20] *AUTODYN Compendium of Papers* (Dnamics, C.; Ed.), USA, **1985**.
[21] Mulligan, P.; Baird, J.; Hoffman, J. The Effects of the Flyer Plate's Radius of Curvature on the Performance of an Explosively Formed Projectile. *Proc. AIP Conference Proceedings*, **2012**, 1426(1): 1023-1026; https://doi.org/10.1063/1.3686452.
[22] Walters, P.; Zukas, J. *Fundamentals of Shaped Charges*. John Wiley & Sons, New York, US, **1989**; ISBN: 0-471-62172-2.
[23] Held, M. Behind Armour Effects at Shaped Charge Attacks. *Proc. 24th Int. Symp. Ballistics,* **2008**; ISBN: 9781932078930.
[24] Elshenawy, T.; Li, Q.M. Breakup Time of Zirconium Shaped Charge Jet. *Propellants Explos. Pyrotech.* **2013**, *38*(5): 703-708; https://doi.org/10.1002/prep.201200191.
[25] Aseltine, C.L. *Analytical Predictions of the Effect of Warhead Asymmetries on Shaped Charge Jets.* Report ADA083437, DTIC, US, **1980**.
[26] Elshenawy, T. Determination of the Velocity Difference between Jet Fragments for a Range of Copper Liners with Different Small Grain Sizes. *Propellants Explos. Pyrotech.* **2015**, *41*(1): 69-75; https://doi.org/10.1002/prep.201500095.
[27] Chou, P.C. Breakup of Shaped Charge Jet. *Proc. 2nd Int. Symp. Ballistics,* Daytona Beach, US-FL, **1976**.
[28] Petit, J.; Jeanclaude, V.; Fressengeas, C. Breakup of Copper Shaped-Charge Jets: Experiment, Numerical Simulations, and Analytical Modeling. *J. Appl. Phys.* **2005**, *98*(12): paper 123521; https://doi.org/10.1063/1.2141647.
[29] Curtis, J.P. A Break-up Model for Shaped Charge Jets. *Proc. 16th Int. Symp. Ballistics,* San Francisco, **1996**.

Received: April 13, 2022
Revised: June 27, 2024
First published online: June 28, 2024